PHYSICAL REVIEW A **86**, 053426 (2012)

Two-electron dynamics in nonlinear double excitation of helium by intense ultrashort extreme-ultraviolet pulses

Chien-Nan Liu,[1] Akiyoshi Hishikawa,[2] and Toru Morishita[3]
[1]*Department of Physics, Fu-Jen Catholic University, Taipei 24205, Taiwan*
[2]*Department of Chemistry, Graduate School of Science, Nagoya University, Aichi 464-8602, Japan*
[3]*Department of Engineering Sciences, University of Electro-Communications, 1-5-1 Chofu-ga-oka, Chofu-shi, Tokyo 182-8585, Japan*

(Received 3 October 2012; published 30 November 2012)

We present a theoretical study for multiphoton double excitation of He atoms exposed to an intense ultrashort extreme-ultraviolet (EUV) pulse, where the photon energy coincides with the transition energy from the ground state to a Rydberg state, by solving the time-dependent Schrödinger equation in the hyperspherical coordinates. Photoelectron spectra under the conditions comparable with a recent experiment [Hishikawa *et al.*, Phys. Rev. Lett. **107**, 243003 (2011)] are calculated and analyzed. We identify the mechanism of the enhanced three-photon absorption probability which is more than one order of magnitude larger than that for the two-photon process in accordance with the experiment. The enhancement is attributed to a propensity rule for double excitation in a two-step mechanism, in which a one-photon absorption by one electron to a Rydberg state is followed by a two-photon absorption by the other electron to an excited orbital, while the first electron remains at nearly the same principle quantum number. Based on the time-dependent perturbation theory, the three-photon absorption probability exhibits peculiar cubic dependence on the pulse duration due to the propensity rule, in contrast to the linear dependence of the two-photon absorption probability. Thus a crossover between the two- and three-photon absorption probabilities takes place for sufficiently intense and long pulses. We also study the time evolution of a doubly excited two-electron wave packet created by an intense ultrashort EUV pulse efficiently using the same enhancement scheme, opening up the possibility of visualizing the correlated motion of two electrons in the time domain.

DOI: 10.1103/PhysRevA.86.053426 PACS number(s): 32.80.Rm, 32.80.Fb, 32.80.Zb

I. INTRODUCTION

Recent advances in high brilliance ultrashort radiation sources in the spectral range of extreme-ultraviolet (EUV) and soft-x-ray regime, notably the developments in high-order harmonic generation (HHG) [1–3] and free electron lasers (FEL) [4–7], have extended studies of nonlinear processes to the short-wavelength regime in the atomic time scale of femto- to subfemtoseconds. Of particular interest is to probe and even control the fundamental dynamics of correlated multielectron systems using such new ultrashort intense radiation sources. As the simplest and most fundamental two-electron system, He provides an ideal system for exploring electron dynamics. Indeed, multiphoton double ionization of He generated by ultrashort intense EUV pulses has attracted considerable attention with many theoretical [8–15] and experimental [16–19] investigations

Compared with double ionization, however, double excitation has not been studied much so far. Since the doubly excited states of He are embedded in the singly ionizing states below the double ionization threshold, they are observed in photoelectron spectra as autoionizing resonances. From the theoretical point of view, such photoelectron spectra can be rigorously calculated by solving the time-dependent Schrödinger equation (TDSE) with the correct asymptotic boundary condition from the standard scattering theory, and can be compared with other calculations and experimental data directly. Moreover, the two electrons in a doubly excited state are affected by each other in a compact space near the nucleus, having a well-defined closed orbital for a long time. Therefore, studies of double excitation are advantageous in analyzing the electron correlations in the time domain.

Several works have dealt with multiphoton double excitation of He with intense ultrashort lasers in the EUV regime. Theoretically, Scrinzi and Piraux [20] used the complex scaling method to solve the TDSE for He in a strong laser field, giving the total ionization yields as a function of laser frequency with peaks below the n-photon threshold attributed to doubly excited resonances. Palacios, Rescigno, and McCurdy [21] solved the TDSE for He under short laser pulses with the exterior complex scaling. Total cross sections for two-photon single ionization are presented and resonances due to doubly excited state were identified in the calculated total ionization yields for multiphoton single ionization. Experimentally, two-photon resonant excitation to the $2p^2\ {}^1S^e$ state by femtosecond high-order harmonic pulses was demonstrated [22]. Similarly, resonant two-photon absorption of FEL radiation to the high-lying doubly excited states in $N \sim 5$ manifolds has been reported [23]. A recent experiment measures the photoelectron spectra corresponding to autoionization of He doubly excited states resulting from three-photon excitation [24], showing that nonlinear double excitation is greatly enhanced by the resonant transition through the intermediate Rydberg states of $1snp$. In this experiment, the photoelectron peak corresponding to three-photon absorption was much greater than the one of two photons, reflecting an interesting nonlinear nature of the process. The enhanced three-photon absorption was attributed to the efficient double excitation by a one-photon resonant transition to a Rydberg state for the outer electron and a subsequent two-photon absorption to excite the inner electron. Resonances due to the doubly excited states converging to the $\text{He}^+(N = 3)$ level were revealed by the shot-by-shot photoelectron spectroscopy and identified by theoretical calculations. However, the mechanism for the dominance of the three-photon ionization yields over the two-photon process as observed in the experimental measurement requires a careful theoretical interpretation. One of the main purposes of this paper is to identify the enhancement mechanism quantitatively with rigorous solutions to the TDSE for He under intense EUV fields.

In addition to the spectroscopic studies in the energy domain, simultaneous excitation of several doubly excited states by an EUV pulse leads to an autoionizing two-electron wave packet, opening up the possibility of studying the correlated electron motions in the time domain. Using the attosecond technology to control and probe the coherent evolution of the wave packet has been suggested as a means to visualize the correlated motion of electrons in He atoms [25]. We explore in the present study an energy region of the spectra where the doubly excited resonances are well separated. Therefore, we can analyze the time evolution of the correlated doubly excited wave packet by examining its density distributions in the hyperspherical coordinates and identifying the moleculelike modes.

In this paper, our focus is to explore the interaction between He atoms and a strong EUV field in the regime where collective excitation due to electron correlation plays an important role. The paper is organized as follows. In Sec. II, we describe the computational method to calculate photoelectron spectra of He atoms exposed to intense EUV pulses using the time-dependent hyperspherical (TDHS) method. We present the theoretical results in Sec. III. The parameters for the EUV pulses are chosen to simulate realistic experimental conditions. The resonances in the spectra are identified and analyzed in Sec. III A. In Sec. III B we present the pulse duration and field intensity dependence of the photoelectron spectra. Enhanced double excitation is observed and its mechanism is identified by an analysis based on the time-dependent perturbation theory in Sec. III C. Owing to a propensity rule for double excitation in a two-step model, the three-photon absorption probability is shown to have a cubic dependence on the pulse dependence, in contrast to the linear dependence of the two-photon absorption probability, thus becoming dominant for sufficiently long and intense pulses. Due to the bandwidth of the EUV pulses, a doubly excited wave packet is efficiently created by a single pulse and its subsequent time evolution is analyzed in Sec. III D. We summarize the paper in Sec. IV. We use atomic units throughout unless otherwise stated.

II. THEORETICAL METHODS

We solve the TDSE,

$$i\frac{\partial}{\partial t}\Psi(t) = [H_0 + V(t)]\,\Psi(t), \tag{1}$$

where H_0 is the Hamiltonian of He atom,

$$H_0 = \sum_{i=1}^{2}\left(-\frac{1}{2}\Delta_i + \frac{2}{r_i}\right) + \frac{1}{|\mathbf{r}_1 - \mathbf{r}_2|} \tag{2}$$

and $V(t)$ is the time-dependent interaction between He and a laser field. We use a linearly polarized field, so the interaction within the dipole approximation in the length form can be expressed as

$$V(t) = (z_1 + z_2)f(t), \tag{3}$$

where the time-dependent electric field is chosen to be

$$f(t) = F_0\cos^2\left(\frac{\pi t}{\tau}\right)\cos\omega t, \tag{4}$$

for $-\tau/2 \leqslant t \leqslant \tau/2$ and zero elsewhere. F_0 is the amplitude of the laser field and the peak intensity is given by $I = \frac{1}{2}\epsilon c F_0^2$ with ϵ being the dielectric constant. $\omega = 2\pi c/\lambda$ is the central angular frequency corresponding to the photon energy with λ being the wavelength. The full width at half maximum (FWHM) of the pulse duration is given by $T = \tau[\cos^{-1}(2^{-1/4})]/\pi = 0.364\tau$.

We solve Eq. (1) by the TDHS method, which is similar to the one used for ion-He collisions [26]. This method contains three steps: (i) Setting up box-normalized basis functions in hyperspherical coordinates. (ii) Solving the time-dependent equation using the box-normalized basis set. (iii) Extracting the transition amplitude by projecting the result of the time propagation onto the eigensolution of the target He atom with the correct boundary condition.

In the TDHS method, the radial distances r_1 and r_2 are replaced by hyperradius $R \in [0,\infty]$ and hyperangle $\alpha \in [0,\pi/2]$ defined by $r_1 = R\cos\alpha$ and $r_2 = R\sin\alpha$, where R stands for the size of the system and α measures the relative distance of the two electrons from the nucleus. In the calculation of the wave functions, we use the spherical angles $\hat{\mathbf{r}}_i = (\theta_i,\phi_i)$ $(i = 1,2)$ of each electron in the laboratory-fixed frame. We will use another set of hyperangular coordinates in the body-fixed frame for the analysis of the wave functions. We obtain the box-normalized eigenfunctions of H_0 within $R \leqslant R_0$ by using the slow-variable discretization (SVD) method [27] based on the discrete variable representation (DVR) method [28] with R as the adiabatic parameter. In this method, the nonadiabatic couplings with respect to R are treated rigorously without laborious calculations. Therefore, the SVD method is advantageous in evaluating the wave functions accurately as well as the matrix elements efficiently in the next step of the time propagation.

We solve the TDSE, Eq. (1), using the second-order split-operator method [29]. Since the dipole transition matrix elements among the box-normalized eigenfunctions should be calculated once for all before the time propagation, the time propagation is carried out efficiently. A similar time-dependent scheme was used in [30].

When the laser field is off at $\tau/2$, we extract the transition amplitude from the time-dependent two-electron wave function $\Psi(\tau/2)$ by projecting onto the eigensolution of the target He atom with correct incoming wave boundary condition, $\Psi^{(-)}_{\mathbf{k}Nlm}$. Here, $\mathbf{k}$ denotes the momentum of the photoelectron, and Nlm are the quantum numbers for the He^+ ion. We calculate the scattering state wave function following the method in [31] with a single hyperradial sector of $R \in [0,R_0]$. In this method, the R matrix at the boundary R_0 is calculated by a spectral resolution of the Green's function with respect to R using the box-normalized eigenfunctions prepared in the first step of the calculation. Then, the S matrix is obtained by carrying out the two-dimensional matching in (R,α) to the asymptotic Coulombic wave function of $\mathrm{He}^+(Nlm) + e^-$ at

$R = R_0$. Thus, the transition amplitude to the final state given by

$$A_{\mathbf{k}Nlm} = \langle \Psi^{(-)}_{\mathbf{k}Nlm} | \Psi(\tau/2) \rangle \tag{5}$$

is calculated using the quadrature rule with respect to R and α efficiently. Then the photoelectron spectra $S_{E_p,Nlm}$ are obtained from

$$S_{E_p,Nlm} = k \int |A_{\mathbf{k}Nlm}|^2 d\hat{\mathbf{k}}, \tag{6}$$

where the integration over $\hat{\mathbf{k}}$ is carried out analytically and $E_p = k^2/2$ is the photoelectron energy. When we plot the photoabsorption spectrum as a function of the total energy E measured from the double ionization threshold, we sum up the spectra for all possible He$^+(Nlm)$ channels, namely,

$$\bar{S}_E = \sum_{Nlm} S_{E_p,Nlm}, \tag{7}$$

with

$$E_p = E + \frac{2}{N^2}. \tag{8}$$

In the actual calculations in the present study, a hyperradial box size of $R_0 = 1600$ a.u. is used so that the reflection of the wave function from the boundary during the time propagation, for the pulse durations considered in this study, is negligible. We have checked the convergence with respect to the number of total angular momentum L included, and confirmed that $L = 0,1,2,3$ are adequate for the laser intensities and durations considered in this paper. As a result, a total number of 120 000 two-electron basis functions are included in the calculations.

III. RESULTS AND DISCUSSIONS

A. Global features of photoelectron spectra

Inspired by the recent experimental work [24], we focus on the photoionization processes of He by intense EUV pulses, where the photon energy coincides with the transition energy to a Rydberg state of He($1snp$). In this subsection, we provide global features of photoelectron spectra obtained by our numerical calculations. Figure 1 gives a schematic diagram, showing two- and three-photon ionization of He from the ground state. While two-photon absorption results only in ionization with He$^+(N = 1) + e^-$, indicated as process (B), three-photon absorption leads to two possible ionization paths with He$^+(N = 2) + e^-$ and He$^+(N = 1) + e^-$ corresponding to processes (A) and (C), respectively. In the experiment, intense FEL EUV pulses with $\lambda \sim 51.4$ nm, $I \sim 5$ TW/cm^2, and $T \sim 100$ fs were used. In Fig. 2, we present calculated photoelectron spectra as functions of photoelectron energy E_p for slightly different laser parameters of $\lambda = 51.202$ nm with $I = 56.2$ TW/cm^2 and $T = 8.29$ fs. In the present work, using the reduced mass of the electron and He$^+$ in order to take into account the mass polarization effects, we apply the conversion factor of 1 a.u. = 27.207 696 eV in computing the photoelectron energy. We choose a photon energy in resonance with the transition from the ground state to the $1s6p$ state, resulting in three-photon absorption to an energy region where doubly excited states of He$^{**}(3lnl')$ are densely located. While a shorter pulse is used in the theoretical study due to the limited computational capacity, a higher intensity is chosen to have a similar laser fluence given by the product of IT.

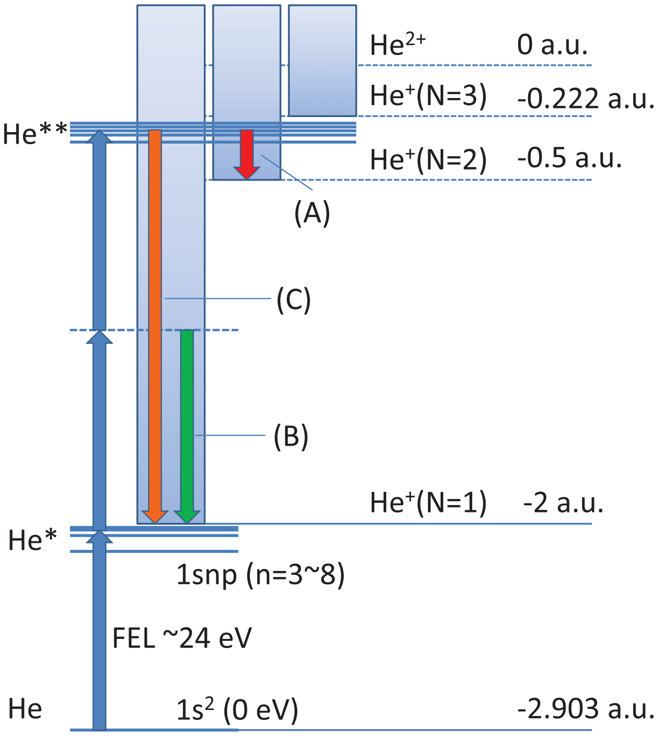

FIG. 1. (Color online) Scheme of three-photon double excitation of He using EUV FEL. (A), (B), and (C) indicate three possible paths by which photoelectrons with different kinetic energies can be observed.

Spectra in logarithmic scale shown in Fig. 2(b) demonstrate rich resonance structures near 7.24 and 48.1 eV corresponding to processes (A) and (C), respectively. A smooth peak centered at 23.8 eV is due to the two-photon absorption corresponding to process (B). Figure 2(a) shows convoluted spectra in linear scale taking into account a finite resolution on experimental photoelectron detection. We use a bias voltage of 6 eV, which is comparable with experimental conditions [24], but a higher energy resolution ($E_p/\Delta E_p = 300$) is adopted to resolve the dominant resonances in the spectra more clearly. Despite the difference in intensities and pulse durations, the overall resonance structure in the convoluted spectrum for process (A) is similar to the experimental observation, although individual resonances were hardly resolved in the experimental spectra due to a lower resolution (cf. Fig. 3 in [24]). We also note that the resonances appear in higher photoelectron energies due to the larger photon energy used in the calculation. The small background in the spectra for both (A) and (C) indicates that autoionization,

$$\text{He} + 3\omega \rightarrow \text{He}^{**} \rightarrow \text{He}^+(N = 1,2) + e^-,$$

dominates over direct ionization,

$$\text{He} + 3\omega \rightarrow \text{He}^+(N = 1,2) + e^-.$$

The integrated areas obtained from the spectra give the probabilities corresponding to these processes, showing the ratio of 1:1/3.7:1/156 among processes (A), (B), and (C). The ratio of 156:1 between the probabilities for processes

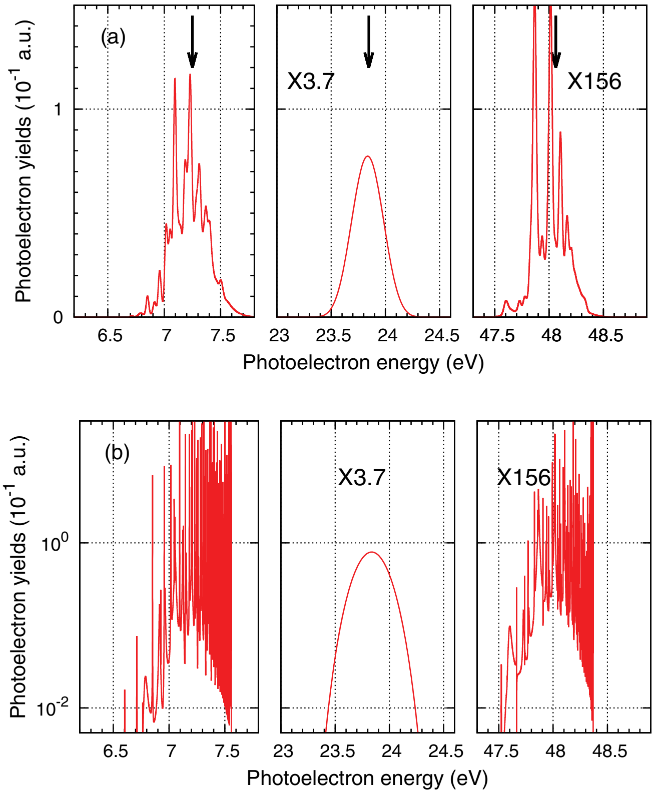

FIG. 2. (Color online) Theoretical photoelectron spectra of He irradiated by an intense EUV laser field with $\lambda = 51.202$ nm, $T = 8.29$ fs, and $I = 56.2$ TW/cm^2. Spectra in left, center, right panels corresponds to ionization processes (A), (B), and (C) illustrated in Fig. 1. Arrows indicate the energies corresponding to two- or three-photon absorption from the ground state for each process. (a) Convoluted spectrum; (b) raw spectrum.

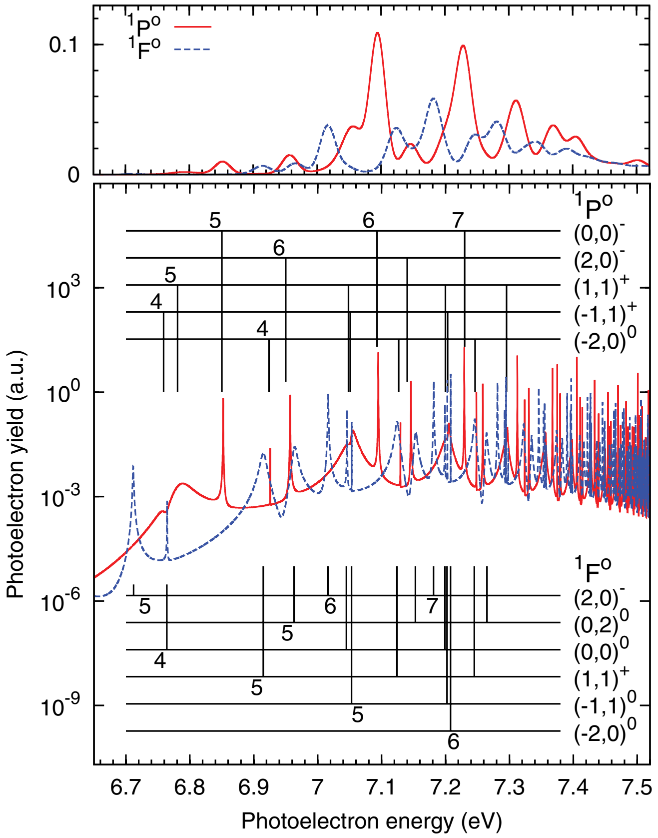

FIG. 3. (Color online) Theoretical photoelectron spectra of He irradiated by an intense laser with $\lambda = 51.202$ nm, $T = 8.29$ fs, and $I = 56.2$ TW/cm^2 for the process of He$(1s^2) + 3\omega \rightarrow$ He$^+(N = 2) + e^-$. The $^1P^o$ (solid red line) and $^1F^o$ (dashed blue line) channels are shown in different colors. Energy positions of the $^1P^o$ and $^1F^o$ doubly excited states converging to the He$^+(N = 3)$ threshold are indicated in the bottom panel. These doubly excited states are labeled with the $(K,T)_n^A$ notation. The photoelectron energy corresponding to three-photon absorption from the ground state is 7.25 eV. The top panel gives the convoluted spectra in linear scale in order to show the relative intensities of the resonances.

(A) and (C) can be understood in terms of the autoionization branching ratios of $10^1 \sim 10^2 : 1$ for He$^+(N = 2) + e^-$ and He$^+(N = 1) + e^-$ [32]. These behaviors are in sharp contrast with one-photon ionization spectra obtained with synchrotron radiation, where the He$^+(N = 1) + e^-$ process has a larger yield with a large background due to the dominance of direct ionization [33]. A more interesting feature in the spectra is that the ratio of 3.7:1 between the probabilities for processes (A) and (B), which is similar to the experimental observation, indicating that three-photon processes are greatly enhanced by the resonant transition through the intermediate Rydberg states. As will be discussed later, the ratio between the three-photon absorption probabilities for $[(\mathrm{A}) + (\mathrm{C})]$ and the two-photon absorption probability for (B) depends on pulse duration and intensity. We will demonstrate how this can be understood based on the time-dependent perturbation theory in the following subsections.

In order to further analyze the characteristics of various resonance series, we plot the partial wave contributions to the photoelectron spectra corresponding to processes (A) in logarithmic scale for the raw spectra and in linear scale for the convoluted spectra in Fig. 3. According to the dipole selection rule, three-photon absorption from the ground state of He$(1s^2\ {}^1S^e)$ leads to $^1P^o$ and $^1F^o$ states. For the classification of the doubly excited states, we adopt the correlation quantum numbers, ${}_N(K,T)_n^A$ [34–39], where N and n denote the principal quantum numbers of the inner and outer electrons, (K,T) represents their angular correlation. A indicates the radial correlation of the two electrons oscillating in phase $(A = +)$ or out of phase $(A = -)$, while $A = 0$ represents states with neither of these properties. We will come back later to the relation of the correlation quantum numbers to the moleculelike motions. The indicated energy positions and the ${}_N(K,T)_n^A$ quantum numbers for the $^1P^o$ resonances are taken from [40]. The classification of the $^1F^o$ resonances is based on the energy positions from [41] and [42]. However, according to the hyperspherical studies in [43], the broad $^1F^o$ resonance near 6.91 eV should be assigned as ${}_3(1,1)_5^+$. As one can see from the convoluted spectra in Fig. 3, all resonance series are almost equally populated with slightly larger yields of ${}_3(0,0)_n^-\ {}^1P^o$ and ${}_3(2,0)_n^-\ {}^1F^o$ states in contrast to the dominance of the selective series of ${}_N(N-2,1)_n^+ = {}_3(1,1)_n^+$ in the single-photon ionization [44]. In addition, in terms of the principal quantum number of the outer electron, the most prominent resonances results from doubly excited states with $n = 6$ or 7. These properties in the three-photon spectra can be attributed to the following two-step excitation model:

$$\mathrm{He}(1s^2) \xrightarrow{\omega} \mathrm{He}(1snp) \xrightarrow{2\omega} \mathrm{He}^{**}(3lvl'), \tag{9}$$

where the first step is a one-photon absorption to bring one $1s$ electron to an np state with $n = 6$ or 7, and the second step takes place by a two-photon transition of the other electron from $1s$ to $3l$ state through the isolated core excitation [45] with the first electron remaining at nearly the same principal quantum number, $\nu \approx n$. Here no significant propensity associated with the $(K,T)^A$ quantum numbers is expected in each step, thus opening up the new pathways to the dense manifold of series of doubly excited states corresponding to different $(K,T)^A$ values to assist the nonlinear double excitations. We will show that the two-step model in Eq. (9) can explain another important observation in the spectra, i.e., the dominance of the three-photon yield over the two-photon yield.

B. Intensity and pulse duration dependence

Nonlinear processes are sensitive to laser parameters. In the shot-by-shot measurements with FEL pulses [24], the intensity and photon energy dependence were studied using the inherent fluctuation of FEL pulses. Since the resonant condition requires matching in energy, one has to take into consideration the finite bandwidth of the ultrashort pulse. Hence, pulse duration dependence provides important information on the multiphoton ionization. In this subsection, we discuss the intensity and pulse duration dependence of one-, two-, and three-photon absorption probabilities as well as the corresponding photoabsorption spectra to reveal the origin of the enhancement of the three-photon absorption processes shown in the previous subsection.

In Fig. 4 we show the intensity dependence for the one-, two-, and three-photon absorption probabilities. Here we use the same pulse duration of $T = 8.29$ fs as in Fig. 2 and a shorter one of $T = 1.38$ fs. These probabilities are obtained from summing/integrating over the photoabsorption spectrum in the corresponding energy regions. Note that the contributions to two different processes (A) and (C) are added up for the three-photon absorption probabilities. Note also that the one-photon process contains the transition to the Rydberg states as well as the low-lying singly ionizing states due to large bandwidths. Clearly, the absorption probabilities corresponding to one-, two-, and three-photon processes are proportional to the powers of intensity, I, I^2, and I^3, respectively, indicating the perturbative nature of the interaction under the given laser parameters. For the longer pulse of $T = 8.29$ fs, the three-photon absorption probability becomes larger than the two-photon absorption probability for $I > 20$ TW/cm^2 as shown in Fig. 4(b). Recall that the ratio between the three- and two-photon absorption probabilities reaches about 3.7 at $I = 56.2$ TW/cm^2 as shown in the previous subsection. Looking into more details, Fig. 5 shows the photoabsorption spectra as functions of total energy E scaled by I^2 and I^3 for the two- and three-photon processes, respectively [cf. Eq. (7)]. The spectra in Fig. 5(b) are convoluted with the energy resolution of $E/\Delta E = 300$ as in Fig. 2(a), but no bias voltage is applied. The resonances corresponding to both process (A) and (C) appear in the total energies of $E \approx -0.2335$ a.u.. In Fig. 5(a), for the two-photon spectra, the peak heights show a small but visible saturation at higher intensities due to a larger ground-state depletion, indicating the perturbative picture would begin to break down at $I \approx 50$ TW/cm^2 for $T = 8.29$ fs. Indeed, the slope of the two-photon probability in Fig. 4(b) is slightly deviated from I^2 at the highest intensity. In the scaled three-photon absorption spectra in Fig. 5(b), small discrepancies in some of the resonances can be also seen for the highest intensity of $I = 56.2$ TW/cm^2 from those for others. Note that, for the shorter pulse of $T = 1.38$ fs, only a very small deviation in the two-photon spectra at the highest intensity of $I = 56.2$ TW/cm^2 is observed.

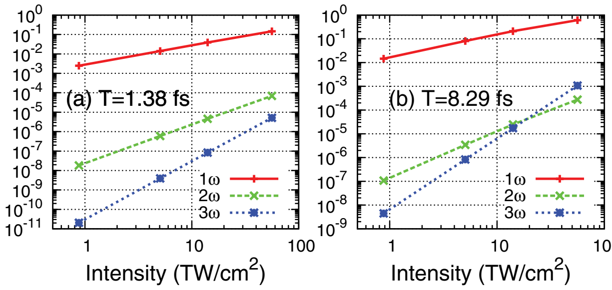

FIG. 4. (Color online) Intensity dependence of the one-, two-, and three-photon absorption probabilities for EUV pulses of $\lambda = 51.202$ nm with two different pulse durations. (a) $T = 1.38$ fs, (b) $T = 8.29$ fs.

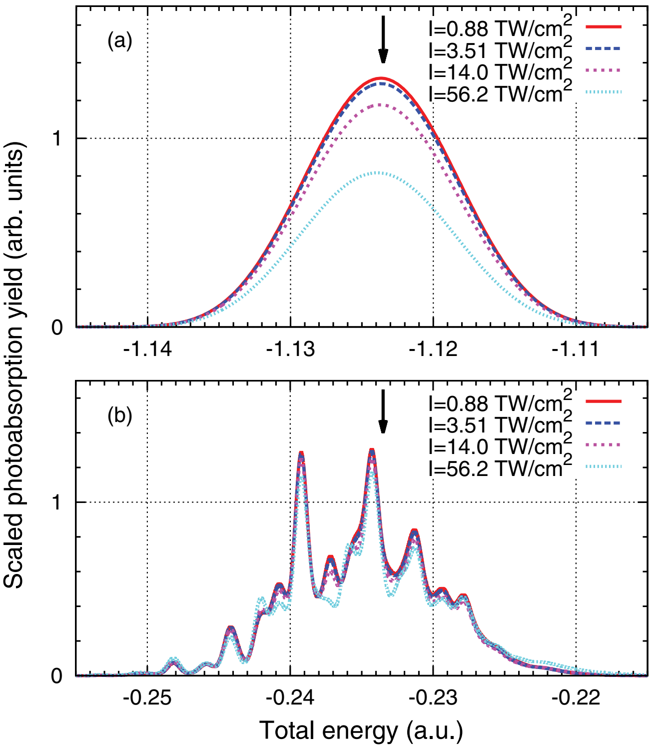

FIG. 5. (Color online) Convoluted photoabsorption spectra of He irradiated by an EUV pulse with $\lambda = 51.202$ nm and $T = 8.29$ fs for different intensities. (a) Scaled with the square of intensity I^2 shown in the energy region corresponding to two-photon absorption from the ground state. (b) Scaled with I^3, shown in the energy region corresponding to three-photon absorption from the ground state.

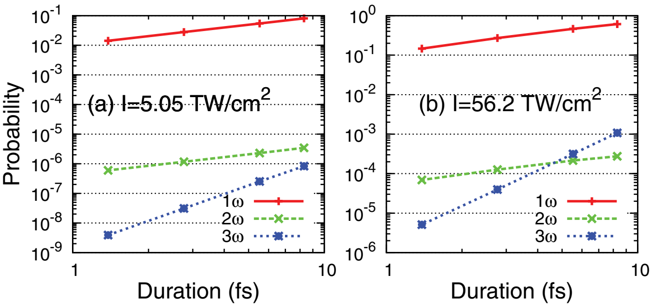

FIG. 6. (Color online) Pulse duration dependence of the one-, two-, and three photon absorption probabilities for EUV pulses of $\lambda = 51.202$ nm with two different intensities. (a) 5.05 TW/cm^2, (b) 56.2 TW/cm^2.

We now turn our analysis to the pulse duration dependence. Figure 6 presents the one-, two-, and three-photon absorption probabilities at the same intensity of $I = 56.2$ TW/cm^2 as in Fig. 2 and a lower intensity of $I = 5.05$ TW/cm^2. For both intensities, the one- and two-photon absorption probabilities scales linearly in T, while the three-photon absorption probabilities shows T^3 dependence. Similar to the intensity dependence, a crossover between the two- and three-photon absorption probabilities can be seen at $T \sim 5$ fs for $I = 56.2$ TW/cm^2. Further examination on the photoabsorption spectra provides a complementary picture for the pulse duration dependence. Figure 7(a) presents the transition probabilities to $1snp$ states divided by the asymptotic energy spacing of $\Delta\omega_n \sim n^{-3}$, which are smoothly connected with the energy normalized photoionization spectra in the continuum at the threshold energy of -2.0 a.u.. It is clearly shown that the peak heights at the resonance energy position is scaled by T^2 and the "spectral width" is proportional to T^{-1}. Consequently, the one-photon transition probability obtained by "integration" over the corresponding energy region is proportional to T as shown in Fig. 6. Similarly, in the two-photon absorption spectra in Fig. 7(b), the T^2 scaling of the peak height and the T^{-1} scaling of the width result in a linear dependence on T in the two-photon absorption probability. On the contrary, the three-photon absorption spectra shows the peak heights scaled by T^4 and the widths by T^{-1} as shown in Fig. 7(c), leading to a higher power dependence of T^3. Note that the spectra in Fig. 7(c) are convoluted with the energy resolution of $E/\Delta E = 300$ without bias voltage.

According to the above studies of intensity and pulse duration dependence based on the rigorous solutions to the TDSE, we can conclude that the one-, two-, and three-photon absorption probabilities for the photon energy in resonance with the $1s6p$ state, $p^{(1)}$, $p^{(2)}$, and $p^{(3)}$, follow the power laws

$$p^{(1)} = a_1 I T, \tag{10a}$$

$$p^{(2)} = a_2 I^2 T, \tag{10b}$$

$$p^{(3)} = a_3 I^3 T^3, \tag{10c}$$

where the coefficients are estimated as $a_1 = 1.9 \times 10^{-3}$ [TW/cm^2 fs]$^{-1}$, $a_2 = 1.6 \times 10^{-8}$ [(TW/cm^2)^2 fs]$^{-1}$, and $a_3 = 9.7 \times 10^{-12}$ [(TW/cm^2)^3 fs^3]$^{-1}$, respectively. As mentioned earlier, the present numerical study is limited to shorter pulse durations compared with the actual FEL. We can estimate the absorption probabilities for the experimental FEL parameters of 5 TW/cm^2 and 100 fs using the power laws. The results are $p^{(1)} = 0.95$, $p^{(2)} = 4.0 \times 10^{-5}$, and $p^{(3)} = 1.2 \times 10^{-3}$, and the ratio of $p^{(3)}/p^{(2)} = 30$ agrees well with the experimentally observed value of 24, although the laser parameters may be close to the limit of validity of the power laws due to the ground-state depletion.

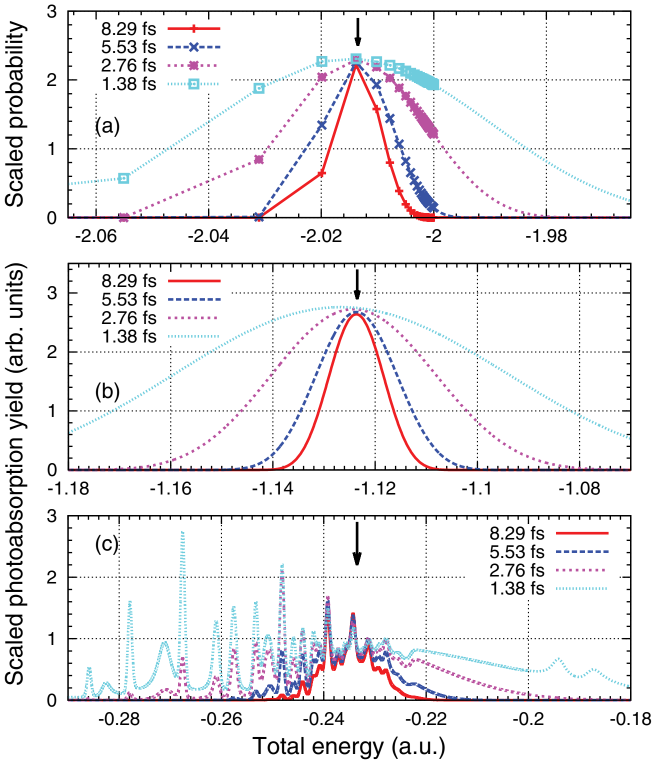

FIG. 7. (Color online) Photoabsorption spectra of He irradiated by an EUV pulse with $\lambda = 51.202$ nm and $I = 5.05$ TW/cm^2 for different pulse durations. (a) One-photon absorption spectra (excitation or ionization probability per unit energy) scaled with the square of the pulse duration T^2. (b) Two-photon absorption spectrum scaled with the square of pulse duration T^2. (c) Three-photon absorption spectra scaled with T^4 and convoluted as in Fig. 5(b). Resonances at -0.194 and -0.188 a.u. are due to the ${}_4(2,1)_4\,{}^1P^o$ and ${}_4(2,1)_4\,{}^1F^o$ doubly excited states, respectively.

C. Analysis based on perturbation theory

In the previous subsection, we studied the intensity and pulse duration dependence of the photoelectron spectra for one-, two-, three-photon absorption, and found the power laws in Eq. (10) based on the accurate TDSE results. In this subsection, we analyze the multiphoton processes in more detail based on the time-dependent perturbation theory. Our analysis reveals that the atomic structure plays a crucial role in the pulse duration dependence of the spectra. More specifically the selective excitations in the second step in Eq. (9) are critical. This will lead us to derive the power laws in Eq. (10) analytically.

The solution to the TDSE may be expanded by the energy eigenstates of He,

$$|\Psi(t)\rangle = \sum\!\!\!\!\!\!\int_j c_j(t)|\varphi_j\rangle e^{-i\omega_j t}, \tag{11}$$

where φ_j is the eigenfunction and ω_j is the corresponding energy. Here, $\sum\!\!\!\!\!\!\int$ is used to denote a summation over discrete states and an energy integration over the energy normalized continuum states as well. In the time-dependent perturbation theory, the expansion coefficient with respect to the jth state for the J-photon absorption, $c_j^{(J)}(t)$, is given by

$$c_j^{(J)}(t) = -iF_0 \sum\!\!\!\!\!\!\!\int_{j'} d_{jj'} \int_{-\infty}^{t} f(t')e^{i\omega_{jj'}t'} c_{j'}^{(J-1)}(t')dt', \qquad (12)$$

for $J \geqslant 1$ and $c_j^{(0)}(t=0) = \delta_{j\mathcal{I}}$, where $\mathcal{I}$ stands for the initial ground state. Here, $d_{jj'} = \langle \varphi_j | z_1 + z_2 | \varphi_{j'} \rangle$ is the dipole transition matrix element, and $\omega_{jj'} = \omega_j - \omega_{j'}$. The transition amplitude and probability are given by $c_j^{(J)} = c_j^{(J)}(t \to \infty)$ and $p_j^{(J)} = |c_j^{(J)}|^2$, respectively. The J-photon absorption probability $p^{(J)}$ is then given by the sum and/or integration of $p_j^{(J)}$ over the corresponding energy region, E_J, i.e., $p^{(J)} = \sum\!\!\!\!\!\!\int_{j \in E_J} p_j^{(J)}$. In the following analysis, we use a laser pulse with a Gaussian envelope,

$$f(t) = F_0 e^{-(t/aT)^2} \cos \omega t, \qquad (13)$$

for simplicity instead of the squared cosine envelope in Eq. (4) used for TDSE calculations. Here $a = (2\ln 2)^{-1/2}$ and T is the FWHM of the Gaussian pulse.

In the present case, one-photon absorption mainly leads to population of the Rydberg states in the vicinity of $1s6p$. The first-order amplitude to the Rydberg $1snp$ states, denoted by n, is simply obtained by carrying out the time integration,

$$\begin{aligned} c_n^{(1)} &= -iF_0 d_{n\mathcal{I}} \int_{-\infty}^{\infty} dt'\, f(t')e^{i\omega_{n\mathcal{I}}t'} \\ &\approx -\frac{i}{2} F_0 d_{n\mathcal{I}} \sqrt{\pi} aT e^{-(\omega-\omega_{n\mathcal{I}})^2 a^2 T^2/4}. \end{aligned} \qquad (14)$$

Here the rotating wave approximation (RWA) is employed. The one-photon absorption probability per unit energy is then given by

$$\frac{p_n^{(1)}}{\Delta\omega_n} \propto \frac{|d_{n\mathcal{I}}|^2}{\Delta\omega_n} IT^2 e^{-(\omega-\omega_{n\mathcal{I}})^2 a^2 T^2/2}, \qquad (15)$$

where I stands for the laser intensity. For large n, the energy spacing is approximated by $\Delta\omega_n \sim n^{-3}$ and the dipole transition matrix element is scaled as $d_{n\mathcal{I}} \propto n^{-3/2}$ [46], so that the squared dipole moment density, $|d_{n\mathcal{I}}|^2/\Delta\omega_n$, becomes constant and smoothly connected to that for the continuum states. Consequently, the peak height and the width for one-photon absorption spectra are scaled as T^2 and T^{-1}, respectively, as shown in Fig. 7(a). Moreover, due to the small energy spacing, the sum over the Rydberg states can be approximated by an energy integral, i.e.,

$$p^{(1)} = \sum_n \frac{p_n^{(1)}}{\Delta\omega_n} \Delta\omega_n \sim \int \frac{p_n^{(1)}}{\Delta\omega_n} d\omega_n, \qquad (16)$$

and extended to the continuum states. As a result, the one-photon absorption probability is given by

$$p^{(1)} \propto IT, \qquad (17)$$

which explains the power law in Eq. (10a). This result is equivalent to Fermi's "golden rule" of perturbation.

Next, we consider the two-photon absorption to the $1s\epsilon s$ and $1s\epsilon d$ states (denoted by ϵ) via the $1snp$ Rydberg states. The transition amplitude with the RWA is given by

$$\begin{aligned} c_\epsilon^{(2)} &= -F_0^2 \sum_n d_{\epsilon n} d_{n\mathcal{I}} \\ &\quad \times \int_{-\infty}^{\infty} dt'\, f(t')e^{i\omega_{\epsilon n}t'} \int_{-\infty}^{t'} dt''\, f(t'')e^{i\omega_{n\mathcal{I}}t''}, \end{aligned} \qquad (18)$$

where the double time integral can be evaluated analytically. Since the dipole transition matrix element between a Rydberg and continuum states is also scaled as $d_{\epsilon n} \propto n^{-3/2}$ with a smooth phase [46], the product $d_{\epsilon n} d_{n\mathcal{I}}/\Delta\omega_n$ should be approximately constant again. The summation over the intermediate Rydberg states, n, can also be approximated by an energy integral. Therefore, denoting $q_{\epsilon\mathcal{I}} = d_{\epsilon n} d_{n\mathcal{I}}/\Delta\omega_n$, we have

$$p_\epsilon^{(2)} \propto I^2 |q_{\epsilon\mathcal{I}}|^2 T^2 e^{-(2\omega-\omega_{\epsilon\mathcal{I}})^2 a^2 T^2/4}. \qquad (19)$$

This result provides the photoabsorption spectrum whose height and width are scaled by T^2 and T^{-1}, respectively, as shown in Fig. 7(b). The two-photon absorption probability, obtained by integrating $p_\epsilon^{(2)}$ over the corresponding energy region, becomes

$$p^{(2)} \propto I^2 T, \qquad (20)$$

which is consistent with the power law in Eq. (10b). Note that the situation is very different from the two-photon single ionization via lower singly excited states of He, where only one or a few intermediate states are contributing due to larger energy separations [47]. In such a case, $p^{(2)}$ is dominated by a component $\propto T^2$ corresponding to the two-photon absorption via a particular single intermediate bound state, and a linear dependence on T would appear in very short pulse durations.

Let us move on to the three-photon absorption. As described earlier, the final states of the three-photon absorption process can be approximately treated as the discrete doubly excited states, since autoionization is the dominant mechanism and direction ionization is negligible. The transition amplitude to the doubly excited state $3l\nu l'$, denoted by ν, is written as

$$\begin{aligned} c_\nu^{(3)} &= iF_0^3 \sum\!\!\!\!\!\!\!\int_{\epsilon n} d_{\nu\epsilon} d_{\epsilon n} d_{n\mathcal{I}} \int_{-\infty}^{\infty} dt'\, f(t')e^{i\omega_{\nu\epsilon}t'} \\ &\quad \times \int_{-\infty}^{t'} dt''\, f(t'')e^{i\omega_{\epsilon n}t''} \int_{-\infty}^{t''} dt'''\, f(t''')e^{i\omega_{n\mathcal{I}}t'''}. \end{aligned} \qquad (21)$$

Here we use the symbol ν for doubly excited states to distinguish them from singly excited states denoted by n. Assuming $d_{\nu\epsilon}$ as well as $d_{\epsilon n}$ are smooth functions of ϵ over a wide range, the triple time integral and the energy integral with respect to ϵ can be carried out analytically. The result reads

$$\begin{aligned} c_\nu^{(3)} &\propto F_0^3 T^2 \sum_n q_{\nu n} d_{n\mathcal{I}} e^{-(\omega_{\nu\mathcal{I}}-3\omega)^2 a^2 T^2/12} e^{-(\omega_{\nu n}-2\omega_{n\mathcal{I}})^2 a^2 T^2/24} \\ &\quad \times \left\{ 1 + \mathrm{erf}\left[i\frac{(\omega_{\nu n} - 2\omega_{n\mathcal{I}})aT}{2\sqrt{6}} \right] \right\}, \end{aligned} \qquad (22)$$

where $q_{\nu n} = d_{\nu\epsilon} d_{\epsilon n}$ is the quadrupole transition matrix element between the Rydberg states of $1snp$ and the doubly excited states $3l\nu l'$, and erf is the Gauss error function. Recall that the two-photon absorption in the two-step model in Eq. (9) is very selective, coupling a $1snp$ Rydberg state to specific doubly excited states of $3l\nu l'$ with $n \approx \nu$. In other words, in the summation of n, $q_{\nu n}$ is significant if $n \approx \nu$, and can be written as

$$q_{\nu n} \sim Q_\nu \delta_{\nu n}, \tag{23}$$

with Q_ν being a constant. Therefore, the summation in Eq. (22) can be reduced to a single term and

$$p_\nu^{(3)} \propto I^3 T^4 |Q_\nu d_{n\mathcal{I}}|^2 e^{-(\omega_{\nu\mathcal{I}}-3\omega)^2 a^2 T^2/6} e^{-(\omega_{\nu n}-2\omega_{n\mathcal{I}})^2 a^2 T^2/12} \times \left\{ 1 + \left| \mathrm{erf}\left[i\frac{(\omega_{\nu n} - 2\omega_{n\mathcal{I}})aT}{2\sqrt{6}} \right] \right|^2 \right\}. \tag{24}$$

This is consistent with the result that the spectra is scaled as T^4 in Fig. 7(c) and the most prominent resonances appearing in the photoelectron spectra corresponding to doubly excited states of $3l\nu l'$ with $\nu = 6$ or 7 as in Fig. 3. Given that the argument of the error function is small, the three-photon absorption probability, obtained by the integration of $p_\nu^{(3)}$ over all doubly excited states, provides at least a cubic dependence on T,

$$p^{(3)} \propto I^3 T^3, \tag{25}$$

which agrees with the power law in Eq. (10c). It is worth noting that if $q_{\nu n}$ is a smooth function of n for each ν, then the summation over the Rydberg states in Eq. (22) would give a factor of T^{-1}. Consequently, the three-photon absorption probability would be proportional to T, and the crossover between the two- and three-photon absorption probabilities would not occur. The properties of the quadrupole transition matrix element $q_{\nu n}$ between the Rydberg states of $1snp$ and the doubly excited states of $3l\nu l'$ as in Eq. (23) is the key to determine the dynamics of the present three-photon process.

In order to verify the structure of $q_{\nu n}$ as given in Eq. (23), we calculate the three-photon transition amplitudes including only a particular Rydberg state n according to the third-order perturbation theory as in Eq. (21). It is clearly seen from the results in Figs. 8(b) and 8(d) that the three-photon absorption via a given Rydberg state $1snp$ primarily leads to population in the doubly excited states of $3l\nu l'$ with either $\nu = n$ or $\nu = n + 1$, confirming that the two-photon excitation is selective as in Eq. (23). In addition, an *incoherent* sum of the photoelectron spectra corresponding to three-photon absorption via all Rydberg states agrees well with the TDSE spectrum as shown in Fig. 8, indicating that the resonant transitions via different Rydberg states would not interfere with each other. Note that, for the laser parameters used, the full calculation based on the third-order perturbation theory, requiring a coherent sum of the transition amplitudes via all intermediate states, actually gives results identical to the TDSE calculations. Therefore, it is confirmed that $q_{\nu n}$ is significant if the outer electron of the intermediate Rydberg state and the final doubly excited state have nearly the same principle quantum number $n \approx \nu$. These findings further support the essence of the two-step model in Eq. (9), i.e., a one-photon excitation to a Rydberg state followed by a two-photon isolated core excitation to a doubly excited state.

To conclude this subsection, it is worth mentioning that, while time-dependent calculations are often limited to pulse durations shorter than the actual ones used in the experiments, the perturbative analysis given above can be useful in comparing theoretical and experimental studies on few-photon multiexcitation or ionization problems. We also comment that it is often assumed that the higher-order amplitudes are much smaller than the lower-order ones, i.e., $|c_j^{(0)}| \gg |c_{j'}^{(1)}| \gg |c_{j''}^{(2)}| \gg \cdots$ in the perturbation theory, but the assumption is unnecessary. Moreover, the assumption is irrelevant in the presence of resonances. In addition, the so-called generalized multiphoton absorption cross section defined by the ionization rate for a monochromatic field within the framework of time-independent approaches is often used to characterize multiphoton-multielectron excitations [48], but it is not suitable for analyzing spectra generated by pulses of finite durations in real experimental situations.

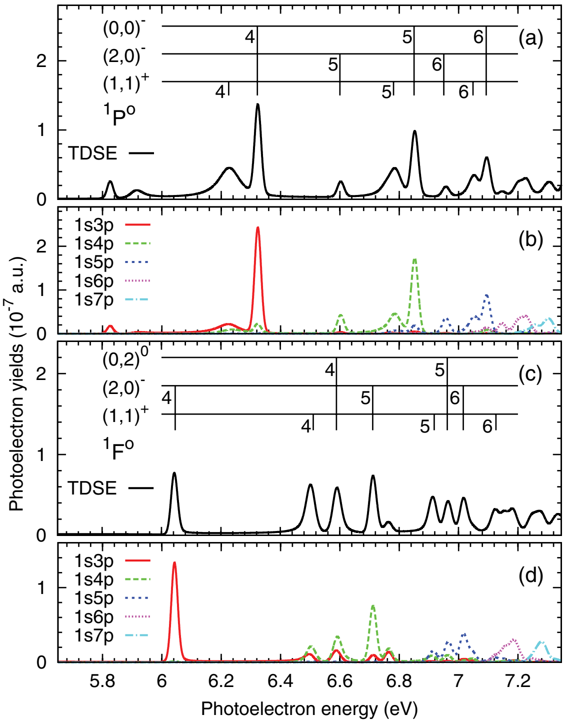

FIG. 8. (Color online) (a) Convoluted photoelectron spectra for the process of He($1s^2$) + $3\omega \rightarrow$ He$^+$($N = 2$) + e^- irradiated by an EUV pulse with $\lambda = 51.202$ nm, $T = 1.38$ fs, and $I = 5$ TW/cm^2 in the $^1P^o$ channel. Results from TDSE and third-order perturbation theory are identical. (b) Convoluted photoelectron spectra in the $^1P^o$ channel as (a), but calculated by the third-order perturbation theory with only transition paths via a specific Rydberg state as indicated. (c) Same as (a) for the $^1F^o$ channel. (d) Same as (b) for the $^1F^o$ channel.

D. Correlated two-electron motions in time domain

Directly probing correlated electronic motions in two-electron atoms in the time domain has been discussed theoretically [25,49], but not yet been realized experimentally. In [25], it is demonstrated that the time-varying moleculelike motion of a doubly excited wave packet can be revealed by measuring doubly ionized electron momentum vectors in coincidence using an attosecond pulse. One of the remaining issues is how to create effectively a well controlled doubly excited wave packet with a realistic laser pulse. In the previous

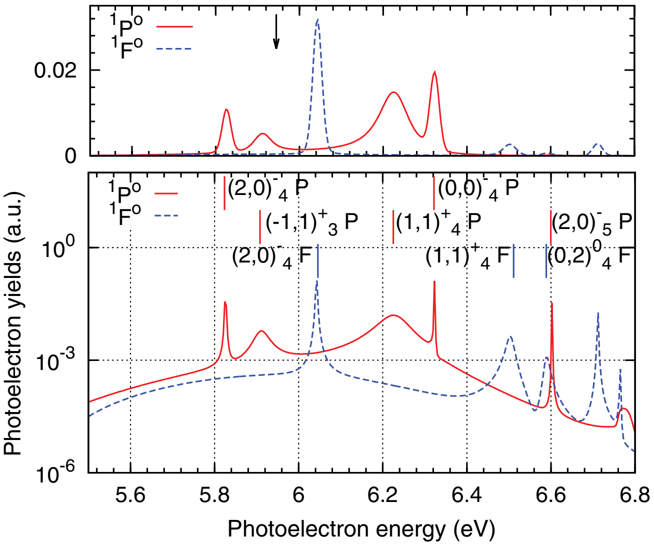

FIG. 9. (Color online) Total and partial photoelectron spectra shown in logarithmic scale for the process of $\mathrm{He}(1s^2) + 3\omega \rightarrow \mathrm{He}^+(N=2) + e^-$ irradiated by an EUV pulse with $\lambda = 52.139$ nm, $T = 5.5$ fs, and $I = 126$ TW/cm^2. The ${}^1P^o$ (solid red line) and ${}^1F^o$ (dashed blue line) components are shown in different colors. Energy positions and corresponding doubly excited states of relevant resonances in this energy region are labeled. The top panel gives the convoluted spectra in linear scale in order to show the relative intensities of the resonances. The arrow in the upper panel indicates the energy position of three-photon absorption from the ground state.

subsections we showed that a coherent doubly excited wave packet composed of $3lnl'$ states can be created very efficiently via the resonant three-photon transition by using intense EUV FEL pulses. In this subsection, we examine the time evolution of the correlated two-electron motions pumped by such an intense laser pulse. In order to make it transparent for analyzing the two-electron wave packet, we study the case with a photon energy close to the $1s4p$ transition since the density of Rydberg states is lower. As a result, only few doubly excited states are populated through three-photon absorption and a wave packet is formed.

For example, we demonstrate in Fig. 9 the photoelectron spectra obtained by a pulse of $\lambda = 52.139$ nm, $T = 5.5$ fs, and $I = 126$ TW/cm^2. We have chosen the photon energy, which is slightly higher than the $1s4p$ resonance transition, in order to demonstrate the wave-packet dynamics clearly. The intensity is just beyond the perturbation regime, so that the scaling laws as discussed in the previous section do not apply. As seen in the photoelectron spectra, five doubly excited states are significantly populated, and the excitation probabilities of these states are listed in Table I. The sum of the double excitation probabilities of 1.4×10^{-4} is less than the experimental result of 1.2×10^{-3} estimated in the previous subsection. In the following, we first examine the correlated two-electron wave functions for those states individually. Then we analyze the time evolution of the two-electron wave packet after the pulse is over.

TABLE I. Probability for exciting the doubly excited resonances in the photoelectron spectrum irradiated by a pulse with $\lambda = 52.139$ nm, $T = 5.5$ fs, and $I = 126$ TW/cm^2. The energy positions indicate the photoelectron energy corresponding to three-photon ionization to $\mathrm{He}^+(N=2) + e^-$ state. Numbers in square brackets indicate powers of 10.

State	Energy position (eV)	Probability
${}_3(2,0)_4^-\,{}^1P^o$	5.824	1.1[−5]
${}_3(-1,1)_3^+\,{}^1P^o$	5.909	1.2[−5]
${}_3(1,1)_4^+\,{}^1P^o$	6.225	6.4[−5]
${}_3(0,0)_4^-\,{}^1P^o$	6.322	1.9[−5]
${}_3(2,0)_4^-\,{}^1F^o$	6.041	3.4[−5]

1. *Vibrational and rotational modes of the constituent doubly excited states*

The characteristics of the two-electron wave functions for the doubly excited states can be visualized by the vibrational and rotational probability density distributions in the hyperspherical coordinates in the body-fixed frame. In Fig. 10, we plot the vibrational and rotational density distributions for those doubly excited states defined by

$$\rho^{\mathrm{vib}}(\Omega_v) = \int |\psi|^2 d\Omega_r dR, \tag{26}$$

$$\rho^{\mathrm{rot}}(\Omega_r) = \int |\psi|^2 d\Omega_v dR, \tag{27}$$

where $\Omega_v = \{\alpha, \theta_{12} = \cos^{-1}(\hat{\mathbf{r}}_1 \cdot \hat{\mathbf{r}}_2)\}$ measures the stretching and bending vibrational motions, and $\Omega_r = (\alpha', \beta', \gamma')$ refers to the three Euler angles to describe overall rotational motions. We choose the body-fixed frame axis as

$$\mathbf{S}_z = \frac{(\hat{\mathbf{r}}_1 - \hat{\mathbf{r}}_2)}{|\hat{\mathbf{r}}_1 - \hat{\mathbf{r}}_2|}, \quad \mathbf{S}_x = \frac{(\hat{\mathbf{r}}_1 \times \hat{\mathbf{r}}_2)}{|\hat{\mathbf{r}}_1 \times \hat{\mathbf{r}}_2|}, \quad \mathbf{S}_y = \frac{(\mathbf{S}_z \times \mathbf{S}_x)}{|\mathbf{S}_z \times \mathbf{S}_x|},$$

with the rotational axis $\mathbf{S}_z$ parallel to the interelectronic axis. Since we are interested in transitions from the ground state of He with $M = 0$, only the $M = 0$ component of the total angular momentum L for the doubly excited states are shown. Note that we plot the rotational density as a function of β' and α', since it does not depend on γ' for $M = 0$. Here ψ contains only the doubly excited component of the wave function, obtained by diagonalizing the He Hamiltonian H_0 in Eq. (2), excluding the lower adiabatic hyperspherical channels converging asymptotically to the $\mathrm{He}^+(N = 1,2)$ thresholds. Therefore, the obtained wave functions exclude the continuum component of the autoionizing states.

Let us examine these distributions for each state in more detail. The $(K,T)^A$ quantum numbers of these states can be related to vibrational and rotational quantum numbers in rovibrational motions of a linear XY_2 molecule, where X stands for the nucleus and Y for the electron [39]. In the molecular picture, $A = \pm$ describes the radial correlation of the two electrons in the symmetric and antisymmetric stretching vibrational modes, respectively. K is related to the bending vibrational quantum number v through the relation $v = N - K - 1$. T corresponds to the projection of the total angular momentum along the rotational axis parallel to the interelectronic axis.

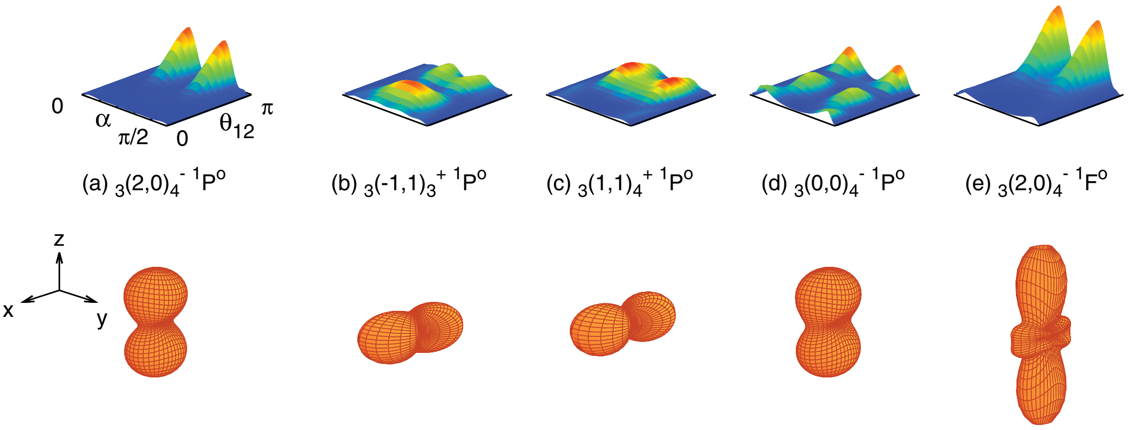

FIG. 10. (Color online) Rotational and vibrational density distribution for the doubly excited states appearing as prominent resonances in the photoelectron spectra in Fig. 9. Upper panel shows vibrational density distributions, $\rho^{\rm vib}(\alpha,\theta_{12})$ in Eq. (26), where α and θ_{12} describe stretching and bending vibrational motions, respectively. Lower panel shows polar plots of rotational density distributions, $\rho^{\rm rot}(\beta',\alpha')$ in Eq. (27), where $\beta' = \cos^{-1}\hat{z}$ and $\alpha' = \tan^{-1}\hat{y}/\hat{x}$ represent polar angles that determine the rotational axis with respect to the interelectronic axis.

From left to right as labeled in Fig. 10, the first four are ${}^1P^o$ states, ordered according to their energy levels, and the last one is a ${}^1F^o$ state. In the following, we would describe them one by one in detail.

(a) For the lowest state, ${}_3(2,0)_4^-\,{}^1P^o$, $\rho^{\rm vib}(\Omega_v)$, has a node at $\alpha = \pi/4$, corresponding to the antisymmetric (or out-of-phase) stretching vibrational mode with $A = -$. In the θ_{12} coordinate, a maximum at $\theta_{12} = \pi$ with no node refers to the ground state in the bending vibrational mode with $v = 0$. $\rho^{\rm rot}(\Omega_r)$ for this state exhibits resemblance to the spherical harmonic $|Y_{LT}(\beta',\alpha')|^2$ with $(L,T) = (1,0)$, indicating a rotationally excited state with its principal axis perpendicular to the interelectronic axis.

(b) The second state, ${}_3(-1,1)_3^+\,{}^1P^o$, is an intrashell state, where the two electrons have the same principal quantum number $N = n = 3$ with $A = +$. One can see two nodal lines at $\theta_{12} = \pi$ and $\sim\pi/2$, corresponding to an excited bending vibrational mode, and antinode at $\alpha = \pi/4$ corresponding to a symmetric mode in stretching vibrational motion. (In the molecular picture, v refers to the number of nodes in the extended region of $0 \leqslant \theta_{12} \leqslant 2\pi$.) Since this state is excited in the bending vibrational mode with $v = 3$, the energy is higher than the intershell state of ${}_3(2,0)_4^-\,{}^1P^o$, which is in the ground state in the bending vibrational mode. Indeed, its energy is the highest among the intrashell states with $N = n = 3$. $\rho^{\rm rot}(\Omega_r)$ for this state exhibits resemblance to $|Y_{11}(\beta',\alpha')|^2$, indicating a rotationally excited state with the principal axis parallel to the interelectronic axis.

(c) The third lowest state, ${}_3(1,1)_4^+\,{}^1P^o$, is an $A = +$ state, exhibiting an antinode at $\alpha = \pi/4$, thus an intershell state in the symmetric stretching vibrational mode. This state is the first excited state with $v = 1$ in $\rho^{\rm vib}(\Omega_v)$, characterized by a nodal line at $\theta_{12} = \pi$. $\rho^{\rm rot}(\Omega_r)$ for this state is similar to the one for ${}_3(-1,1)_3^+\,{}^1P^o$, thus having the same rotational properties.

(d) The fourth state, ${}_3(0,0)_4^-\,{}^1P^o$, has one additional nodal line at $\theta_{12} \sim 2\pi/3$ in comparison with ${}_3(2,0)_4^-\,{}^1P^o$, representing a higher excited state in bending vibrational motion with $v = 2$. This is an intershell state in an antisymmetric stretching vibrational mode, as indicated by the $A = -$. Its rotational properties are similar to that of ${}_3(2,0)_4^-\,{}^1P^o$, characterized by $|Y_{10}(\beta',\alpha')|^2$.

(e) $\rho^{\rm vib}(\Omega_v)$ for ${}_3(2,0)_4^-\,{}^1F^o$ is similar to that for ${}_3(2,0)_4^-\,{}^1P^o$ as expected from the same $(K,T)^A$ quantum numbers. The difference is in $\rho^{\rm rot}(\Omega_r)$; the one of ${}_3(2,0)_4^-\,{}^1F^o$ is dominated by $|Y_{30}(\beta',\alpha')|^2$.

2. Time evolution of the doubly excited wave packet

Let us turn to our discussion on the time evolution of the wave packet based on the molecular picture. Figures 11 and 13 show the time evolution of $\rho^{\rm vib}(\Omega_v)$ and $\rho^{\rm rot}(\Omega_r)$ of the wave packet after the EUV pulse is over. Since we are interested in probing the doubly excited wave packet, we exclude the ground and singly excited states as well as continuum components of the autoionizing states as described earlier for the doubly excited states shown in Fig. 10. Indeed, in the probing process as discussed in [25], the contribution from the ground and singly excited states can be distinguished in terms of photoelectron energy, and the interaction between the probe pulse and the continuum part is weak, compared with the doubly excited part. As a result, the density distributions shown in Figs. 11 and 13 can be understood as a coherent superposition of those presented in Fig. 10. In the actual calculations of the time-dependent densities, we propagate the wave function for a long enough time after the pulse vanishes with an absorbing boundary condition, which is imposed by multiplying the hyperradius function at the end of each time step with a masking function,

$$g(R) = \begin{cases} \cos\left(\frac{\pi}{2}\frac{R-R_m}{R_0-R_m}\right) & \text{for} \quad R \geqslant R_m, \\ 1 & \text{for} \quad R < R_m, \end{cases}$$

with $R_m = 0.95R_0$, in order to ensure that the wave function is not distorted by reflections from the boundary. Note that the doubly excited component is confined in the regime of small hyperradius R and thus is not affected by the masking procedure.

Let us consider $\rho^{\rm vib}(\Omega_v)$ in Fig. 11. To give a quantitative measure of the bending vibrational motion of the wave packet,

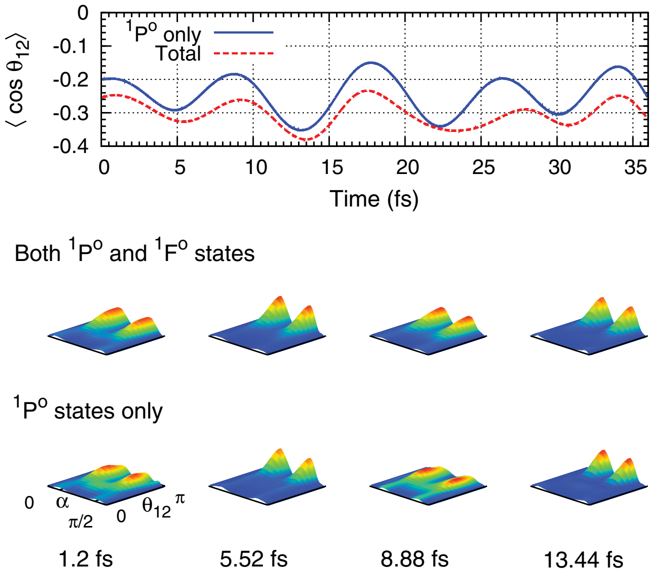

FIG. 11. (Color online) Time evolution of the expectation values of $\langle\cos\theta_{12}\rangle$ after the laser pulse is over at time of zero. $\langle\cos\theta_{12}\rangle$ using only the ${}^1P^o$ states is shown along with the one obtained including all the states. Vibrational density distributions from the ${}^1P^o$ component only (bottom) and the full wave function (top) at several different times are also plotted. In the calculations for the expectation values and the density distribution, the hyperspherical channels converging to the $\mathrm{He}^+(N=1,2)$ thresholds are removed from the wave function. Convolution is carried out to average out the fast oscillation due to remnant contributions from Rydberg states.

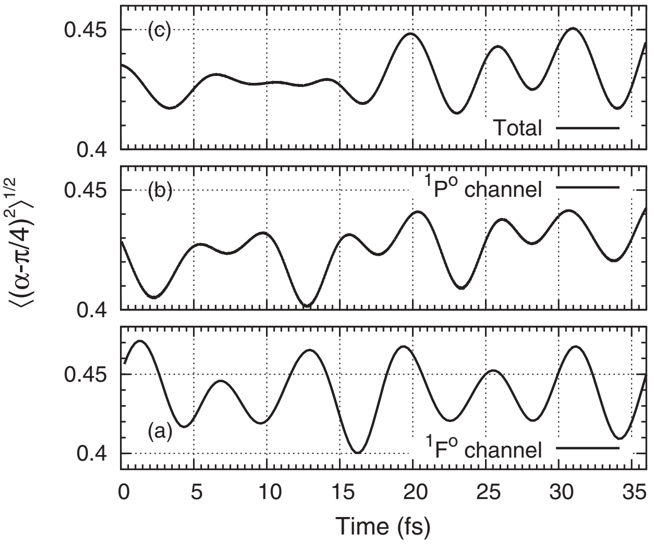

FIG. 12. Time evolution of the standard deviation of α about $\pi/4$, $\langle(\alpha-\pi/4)^2\rangle^{1/2}$ calculated from (a) the ${}^1F^o$, (b) the ${}^1P^o$ components, and (c) the full wave function. In the calculations for the expectation values, the hyperspherical channels converging to the $\mathrm{He}^+(N=1,2)$ thresholds are removed from the wave function. Convolution is carried out to average out the fast oscillation due to remnant contributions from Rydberg states.

we also plot the expectation value of $\langle\cos\theta_{12}\rangle$ in the figure. Since the different total angular momentum contributions are decoupled in $\rho^{\mathrm{vib}}(\Omega_v)$, we first focus on the ${}^1P^o$ component only. A clear oscillating period of 8.25 fs can be attributed to the coherent sum of the ${}_3(2,0)_4^-\,{}^1P^o$ and ${}_3(0,0)_4^-\,{}^1P^o$ states with different K's. For $\rho^{\mathrm{vib}}(\Omega_v)$ including the ${}^1F^o$ component, one can recognize that a large contribution from the ${}_3(2,0)_4^-\,{}^1F^o$ state is added incoherently, since this is the only ${}^1F^o$ state significantly excited. We can also observe that $\langle\cos\theta_{12}\rangle$ is not monochromatic due to contributions from other states. Other frequency components will become discernible if the time evolution of $\langle\cos\theta_{12}\rangle$ is analyzed for a much longer period.

Next, we examine the time evolution of the stretching vibrational motion in α. Figure 12 shows the time dependence of the standard deviation of α about $\pi/4$, $\langle(\alpha-\pi/4)^2\rangle^{1/2}$. The time dependence is quite complicated with a small amplitude [cf. Fig. 12(c)], since more states are strongly coupled in the stretching vibrational motion. Therefore, probing the stretching vibrational mode of such a wave packet would not be easy. Similar to the motion in θ_{12}, we consider the α motions for ${}^1P^o$ and ${}^1F^o$ separately. The ${}^1P^o$ component in Fig. 12(b) shows a beating between two frequencies with a ratio ∼2. A characteristic period of 10.36 fs, corresponding to the energy spacing between two $A=\pm$ states of ${}_3(2,0)_4^-\,{}^1P^o$ and ${}_3(1,1)_4^+\,{}^1P^o$, can be identified. The higher frequency component involves ${}_3(2,0)_4^-\,{}^1P^o$ and a higher excited state, ${}_3(2,0)_5^-\,{}^1P^o$, which is much less populated, giving a smaller amplitude modulation. Coincidentally, the ${}^1F^o$ component in Fig. 12(a) also shows beating with a frequency ratio of 2:3, also involving higher but weakly populated states as in the ${}^1P^o$ component.

Last we discuss the time evolution of $\rho^{\mathrm{rot}}(\Omega_r)$. The standard deviation of β' about $\pi/2$, $\langle(\beta'-\pi/2)^2\rangle^{1/2}$, gives a quantitative measure for the rotational motion of the wave packet with the larger value corresponding to the smaller angle between the rotation axis and the interelectronic axis. The time evolution of $\langle(\beta'-\pi/2)^2\rangle^{1/2}$ is shown in Fig. 13 along with $\rho^{\mathrm{rot}}(\Omega_r)$ of the wave packet at several different instances. One can extract

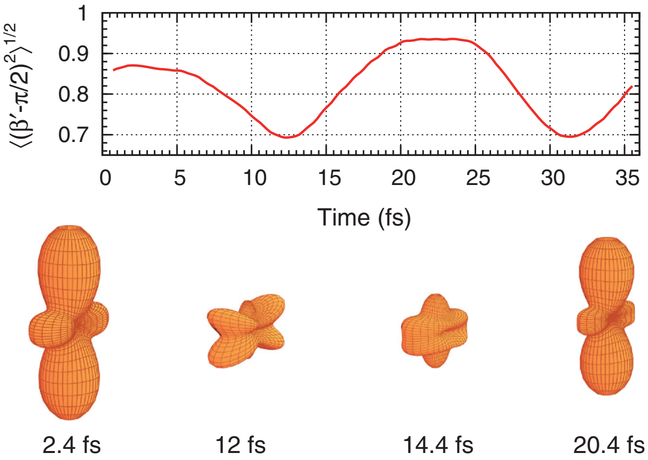

FIG. 13. (Color online) Time evolution of the standard deviation of β' about $\pi/2$, $\langle(\beta'-\pi/2)^2\rangle^{1/2}$. Polar plots for the density distribution of the rotational wave functions at several different times are also plotted. In the calculations for the expectation values and the probability density, hyperspherical channels converging to the $\mathrm{He}^+(N=1,2)$ thresholds are removed from the wave function for better visibility. Convolution is carried out to average out the fast oscillation due to remnant contributions from Rydberg states.

an oscillation period of approximately 19 fs corresponding to the energy spacing between the two prominent components of $_3(2,0)_4^- \; ^1P^o$ and $_3(2,0)_4^- \; ^1F^o$ states with the same (K,T) but different L's. Contributions from other states are much less visible due to the small overlap in the wave functions with different $(K,T)^A$ quantum numbers.

The oscillating periods of the rovibrational molecular motions demonstrated above are of the order of a few femtoseconds, so that it would be feasible to extract those correlated motions by measuring doubly ionized electron momenta using an attosecond pulse [25].

IV. SUMMARY

We have presented a theoretical study for multiphoton ionization of He, where the photon energy equals to the transition energy from the ground state to the $1s6p\ ^1P^o$ Rydberg state. Accurate theoretical photoelectron spectra are shown by solving the time-dependent Schrödinger equation rigorously with the time-dependent hyperspherical method. Taking into account the experimental resolution, convoluted spectra are presented, giving qualitative agreement with experimental measurements. Detailed features of resonance structures could be resolved if the experimental resolution is high enough, using shot-by-shot photoelectron spectroscopy. We discussed the intensity and pulse duration dependence of the photoabsorption spectra and probabilities, providing insights into modeling the nonlinear processes involving matter exposed to EUV or x-ray laser fields. Using a two-step model for the three-photon process, in which one-photon resonant excitation from the ground state to the $1snp$ Rydberg state is followed by a two-photon transition of the inner electron to the $3l\nu l'$ states with $\nu \approx n$, we showed the three-photon absorption probability scales as I^3T^3, while two-photon probability scales as I^2T. These power laws explain why the three-photon absorption probability would dominate for sufficiently intense and longer pulses. The power laws also explain the experimental value of the ratio between the three- and two-photon absorption probabilities. The propensity, where the transition is significant with nearly the same principal quantum number $\nu \approx n$ during the second step, plays a very important role. The crossover between the two- and three-photon probabilities would not occur without this propensity. This study demonstrates that, in addition to the direct manifestation in the spectral width, pulse duration is a laser parameter that can be used to probe the dynamics, giving different power laws of the photoelectron spectra. The T^3 dependence can actually be generalized to describe multiphoton absorption probability of double excitation via intermediate Rydberg states in a two-step manner, regardless of the number of photons involved in each step, given that the transition between the intermediate Rydberg states and the final doubly excited states is selective. For example, such conditions are generally satisfied by isolated core excitation (ICE) processes.

Furthermore, the multiphoton absorption could create a doubly excited wave packet efficiently, opening up the possibility to probe the ultrafast motion of the correlated electrons directly in a pump-probe scheme. We have shown an example of the time evolution of a wave packet created by three-photon absorption in resonance with the $1s4p$ state, in which both the bending vibrational and rotational modes of the two-electron motion can be demonstrated and resolved. However, since the stretching vibrational modes are more strongly coupled, it would require a more selective excitation scheme to generate a wave packet in which the stretching vibrational modes can be resolved.

ACKNOWLEDGMENTS

This work was supported by a Grant-in-Aid for Scientific Research (C) from the Ministry of Education, Culture, Sports, Science and Technology, Japan. C.N.L. acknowledges support from the National Science Council, Taiwan, under Grant No. NSC 98-2112-M-030-001-MY3. T.M. thanks O. I. Tolstikhin and L. B. Madsen for fruitful discussions and comments.

---

[1] T. Sekikawa, A. Kosuge, T. Kanai, and S. Watanabe, Nature (London) **432**, 605 (2004).
[2] G. Sansone, E. Benedetti, F. Calegari, C. Vozzi, L. Avaldi, R. Flammini, L. Poletto, P. Villoresi, C. Altucci, R. Velotta, S. Stagira, S. De Silvestri, and M. Nisoli, Science **314**, 443 (2006).
[3] E. Goulielmakis, M. Schultze, M. Hofstetter, V. S. Yakovlev, J. Gagnon, M. Uiberacker, A. L. Aquila, E. M. Gullikson, D. T. Attwood, R. Kienberger, F. Krausz, and U. Kleineberg, Science **320**, 1614 (2008).
[4] W. Ackermann *et al.*, Nat. Photon. **1**, 336 (2007).
[5] T. Shintake *et al.*, Nat. Photon. **2**, 555 (2008).
[6] B. McNeil, Nat. Photon. **3**, 375 (2009).
[7] T. Ishikawa *et al.*, Nat. Photon. **6**, 540 (2012).
[8] M. Kurka *et al.*, New J. Phys. **12**, 073035 (2012), and references therein.
[9] Z. Zhang, L.-Y. Peng, M.-H. Xu, A. F. Starace, T. Morishita, and Q. Gong, Phys. Rev. A **84**, 043409 (2011).
[10] Z. Zhang, L.-Y. Peng, Q. Gong, and T. Morishita, Opt. Express **18**, 8976 (2010)
[11] E. Foumouo, A. Hamido, Ph. Antoine, B. Piraux, H. Bachau, and R. Shakeshaft, J. Phys. B **43**, 091001 (2010).
[12] R. Pazourek, J. Feist, S. Nagele, E. Persson, B. I. Schneider, L. A. Collins, and J. Burgdörfer, Phys. Rev. A **83**, 053418 (2011).
[13] A. Palacios, D. A. Horner, T. N. Rescigno, and C. W. McCurdy, J. Phys. B **43**, 194003 (2010).
[14] I. A. Ivanov and A. S. Kheifets, Phys. Rev. A **79**, 023409 (2009).
[15] P. Lambropoulos, G. M. Nikolopoulos, and K. G. Papamihail, Phys. Rev. A **83**, 021407 (2011).
[16] H. Hasegawa, E. J. Takahashi, Y. Nabekawa, K. L. Ishikawa, and K. Midorikawa, Phys. Rev. A **71**, 023407 (2005).
[17] A. A. Sorokin, M. Wellhöfer, S. V. Bobashev, K. Tiedtke, and M. Richter, Phys. Rev. A **75**, 051402 (2007).
[18] R. Moshammer *et al.*, Phys. Rev. Lett. **98**, 203001 (2007).
[19] A. Rudenko *et al.*, Phys. Rev. Lett. **101**, 073003 (2008).
[20] A. Scrinzi and B. Piraux, Phys. Rev. A **58**, 1310 (1998).

[21] A. Palacios, T. N. Rescigno, and C. W. McCurdy, Phys. Rev. A **77**, 032716 (2008); **79**, 033402 (2009).
[22] T. Sekikawa, T. Okamoto, E. Haraguchi, M. Yamashita, and T. Nakajima, Opt. Express **16**, 21922 (2008).
[23] M. Nagasono, E. Suljoti, A. Pietzsch, F. Hennies, M. Wellhöfer, J.-T. Hoeft, M. Martins, W. Wurth, R. Treusch, J. Feldhaus, J. R. Schneider, and A. Föhlisch, Phys. Rev. A **75**, 051406(R) (2007).
[24] A. Hishikawa, M. Fushitani, Y. Hikosaka, A. Matsuda, C.-N. Liu, T. Morishita, E. Shigemasa, M. Nagasono, K. Tono, T. Togashi, H. Ohashi, H. Kimura, Y. Senba, M. Yabashi, and T. Ishikawa, Phys. Rev. Lett. **107**, 243003 (2011).
[25] T. Morishita, S. Watanabe, and C. D. Lin, Phys. Rev. Lett. **98**, 083003 (2007).
[26] T. Morishita, K. Hino, T. Edamura, D. Kato, S. Watanabe, and M. Matsuzawa, J. Phys. B **34**, L475 (2001).
[27] O. I. Tolstikhin, S. Watanabe, and M. Matsuzawa, J. Phys. B **29**, L389 (1996).
[28] D. O. Harris, G. G. Engerholm, and W. D. Gwinn, J. Chem. Phys. **43**, 1515 (1965); A. S. Dickinson and P. R. Certain, *ibid.* **49**, 4209 (1968); J. C. Light and R. B. Walker, *ibid.* **65**, 4272 (1976); J. C. Light, I. P. Hamilton, and J. V. Lill, *ibid.* **82**, 1400 (1985).
[29] M. D. Feit, J. A. Fleck, Jr., and A. Steiger, J. Comput. Phys. **47**, 412 (1982)
[30] X. M. Tong and C. D. Lin, Phys. Rev. A **71**, 033406 (2005).
[31] D. Kato and S. Watanabe, Phys. Rev. A **56**, 3687 (1997).
[32] I. Sanchez and F. Martin, Phys. Rev. A **44**, 7318 (1991).
[33] A. Menzel, S. P. Frigo, S. B. Whitfield, C. D. Caldwell, and M. O. Krause, Phys. Rev. A **54**, 2080 (1996).
[34] D. R. Herrick and O. Sinanoğlu, Phys. Rev. A **11**, 97 (1975).
[35] M. E. Kellman and D. R. Herrick, J. Phys. B **11**, L755 (1978).
[36] O. Sinanoğlu and D. R. Herrick, J. Chem. Phys. **62**, 886 (1975).
[37] M. E. Kellman and D. R. Herrick, Phys. Rev. A **22**, 1536 (1980).
[38] G. S. Ezra and R. S. Berry, Phys. Rev. A **28**, 1974 (1983).
[39] C. D. Lin, Adv. At. Mol. Phys. **22**, 77 (1986).
[40] Y. K. Ho, Phys. Rev. A **44**, 4154 (1991).
[41] Y. K. Ho, J. Phys. B **31**, 3307 (1998).
[42] L. Lipsky, R. Anania, and M. J. Conneely, At. Data Nucl. Data Tables **20**, 127 (1977).
[43] C. D. Lin, Phys. Rev. A **29**, 1019 (1984).
[44] J. M. Rost and J. S. Briggs, J. Phys. B **23**, L339 (1990); H. R. Sadeghpour and C. H. Greene, Phys. Rev. Lett. **65**, 313 (1990); A. Vollweiter, J. M. Rost, and J. S. Briggs, J. Phys. B **24**, L155 (1991); J. M. Rost, K. Schulz, M. Domke, and G. Kaindl, *ibid.* **30**, 4663 (1997).
[45] W. E. Cooke, T. F. Gallagher, S. A. Edelstein, and R. M. Hill, Phys. Rev. Lett. **40**, 178 (1978).
[46] H. A. Bethe and E. E. Salpeter, *Quantum Mechanics of One- and Two-electron Atoms* (Dover, New York, 2008).
[47] K. L. Ishikawa and K. Ueda, Phys. Rev. Lett. **108**, 033003 (2012).
[48] P. Lambropoulos, P. Margagakis, and J. Zhang, Phys. Rep. **305**, 203 (1998).
[49] S. X. Hu and L. A. Collins, Phys. Rev. Lett. **96**, 073004 (2006).